Semiconductor Surface Plasmon Sources

A. Babuty,[1] A. Bousseksou,[2,*] J.-P. Tetienne,[2] I. Moldovan Doyen,[1] C. Sirtori,[3] G. Beaudoin,[4] I. Sagnes,[4]
Y. De Wilde,[1] and R. Colombelli[2,†]

[1]*Institut Langevin, ESPCI ParisTech, CNRS UMR 7587, LOP, 75005 Paris, France*
[2]*Institut d'Electronique Fondamentale, Université Paris-Sud and CNRS, UMR8622, 91405 Orsay, France*
[3]*Laboratoire MPQ, Université Paris Diderot and CNRS, UMR7612, 75013 Paris, France*
[4]*CNRS/LPN, Laboratoire de Photonique et de Nanostructures, 91460 Marcoussis, France*

Surface-plasmon polaritons (SPPs) are propagating electromagnetic modes bound at a metal-dielectric interface. We report on electrical generation of SPPs by reproducing the analogue in the near field of the slit-doublet experiment, in a device which includes all the building blocks required for a fully integrated plasmonic active source: an electrical generator of SPPs, a coupler, and a passive metallic waveguide. SPPs are generated upon injection of electrical current, and they are then launched at the edges of a passive metallic strip. The interference fringes arising from the plasmonic standing wave on the surface of the metallic strip are unambiguously detected with apertureless near-field scanning optical microscopy.

Recent interest in surface-plasmon polaritons (SPPs) stems from promising applications, such as integrated plasmonics [1] and nanosensing [2,3]. Integrated plasmonics is expected to provide a technology capable of confining light over extreme subwavelength dimensions, thus bridging fast—but diffraction-limited—photonics and highly integrated electronics [4]. A fundamental issue still not completely solved is how to efficiently generate and launch SPPs into passive plasmonic waveguides [5]. This is generally achieved by coupling light from free space or from conventional optical waveguides into plasmonic structures, for instance by prism-coupling, fiber coupling, or—very recently—using nonlinear four-wave mixing [6]. A compact electrical source capable of generating SPPs onto passive components would represent a crucial step, for instance as building-block for plasmonic circuitry and interconnections.

Here, we demonstrate an electrically injected semiconductor SPP laser source. Periodically patterning the top metallic contact of a midinfrared quantum cascade laser (QCL) allows us to couple the electromagnetic wave propagating at the semiconductor-metal interface with that of the metal-air interface. The SPPs at the top air-metal interface profits from the optical gain experienced by the SPP on the other semiconductor side [7]. We are then able to launch them—in counterpropagating directions—into a passive section (a metallic strip). This is essentially the electrical analogue of the slit-doublet experiment recently revisited in the near field [8,9]. Importantly, for efficient injection of SPPs into the passive section, the SPP wave vectors must be matched, and this is the role of the integrated grating couplers, as schematized in Fig. 1(a). The device includes the three basic components required for a fully integrated plasmonic component: an electrical generator of SPPs, a coupler, and a passive metallic waveguide. This is demonstrated here for a device operating at

$\nu_{laser} = 40$ THz ($\lambda = 7.5$ μm). We show—by characterizing the device with an apertureless near-field scanning optical microscope (a-NSOM)—that SPPs are injected into the passive section only when the grating coupler is present.

The semiconductor samples (InP238) [10] are surface-plasmon QCLs [11] designed for nominal emission at $\lambda = 7.5$ μm. The devices were fabricated into 22-μm-wide, 4-μm-deep mesa ridges, whose top, gold metallic surface is patterned via electron-beam lithography followed by lift-off [Figs. 1(c)]. More details can be found in the supplemental material [12].

The active parts of the device are the two 1st order distributed feedback (DFB) laser sections [Fig. 1(a)], which make use of an air-metal top grating to achieve distributed feedback, as described in [7]. In order to achieve laser action, the 50%-duty-cycle grating stop band is overlapped with the active material optical gain by carefully tuning the grating period Λ, which ranges from 1.176 to 1.224 μm. In these sections, standing electromagnetic waves of frequency $\nu_{laser} = c/\lambda$ are present with a momentum $\beta_{laser} = (2\pi/\lambda)n_{eff} = \pi/\Lambda$, where n_{eff} is the effective index of the lasing mode, λ is the free-space wavelength, and c is the speed of light in vacuum [Fig. 1(b), continuous blue curve and inset]. The passive part of the device is a metallic strip of length L_{strip} and thickness 80 nm, well above the gold skin depth at $\lambda = 7.5$ μm, which is ≈ 10 nm. L_{strip} was set to 50 times the DFB grating period ($L_{strip} = 50\Lambda$). It is long enough to contain a few times the wavelength of a 40 THz SPP wave propagating on the strip metallic top surface, as in the slit-doublet experiment, in order to allow clear interference fringes observation. Note that in our frequency range the SPP dispersion yields $\lambda_{spp} \approx \lambda$, as it is very close to the light line [Fig. 1(b)]. Furthermore, the SPP decay length at midinfrared wavelengths is much longer than the strip length. For instance, using the com-
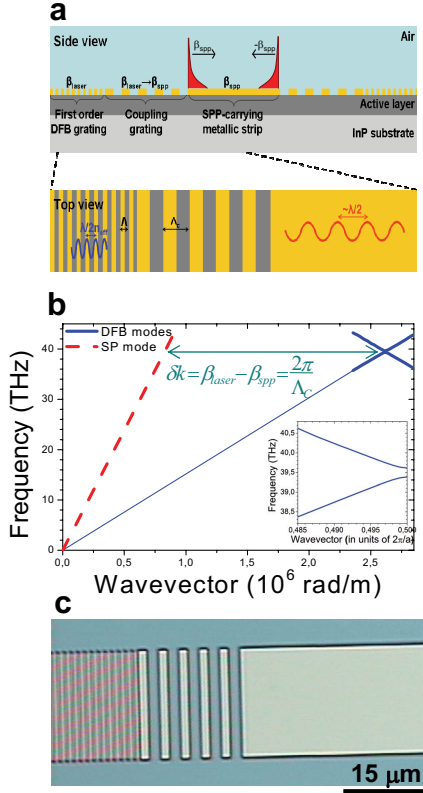
FIG. 1 (color online). (a) Schematics of the device. The upper (lower) image represents a view from the side (top), respectively. It is composed by two symmetric generation sections, two symmetric couplers, and a passive central metallic strip. SPPs are generated in the first ones, and launched into the passive section—with opposing wave vectors $+\beta_{\rm spp}$ and $-\beta_{\rm spp}$—thanks to the couplers. (b) Calculated photonic-band structure for an infinite surface-plasmon DFB on the QCL structure employed in this work (continuous blue curve). The grating duty-cycle is 50%, and its period is 1.2 μm. The dashed red curve is the dispersion of a SPP excitation bound at an air-gold interface. Inset: close-up of the DFB dispersion at the zone edge, where lasing is expected to occur. (c) Microscope image of the device "core" showing the DFB grating, the coupler, and part of the metallic strip.

plex dielectric function for gold at $\lambda \approx 8$ μm [13], an estimate yields

$$\frac{1}{\alpha_{\rm spp}} = \lambda \frac{\epsilon_1^2}{2\pi\epsilon_2\epsilon_d^{3/2}} \approx 2.6 \text{ cm}, \tag{1}$$

where $\alpha_{\rm spp}$ is the SPP attenuation coefficient. Note that in Ref. [14], where excitation of SPPs was demonstrated in a system based on organic light-emitting diodes, the propagation length was only 2 μm, due to the gigantic Ohmic losses at $\lambda \approx 700$ nm. Furthermore, the semiconductor-based approach presented in this Letter is advantageous since the large optical gains typical of semiconductor lasers can be exploited. The propagation constant of SPPs traveling on the metallic strip is $\beta_{\rm spp} = 2\pi/\lambda_{\rm spp} \approx 2\pi/\lambda$ [Fig. 1(b)]. For efficient injection of SPPs into the passive section, the two different momenta—$\beta_{\rm laser}$ and

$\beta_{\rm spp}$—must be matched: it is the role of the integrated grating couplers [Fig. 1(a)]. They are 5-period 50%-duty-cycle gratings, whose period Λ_C satisfies the matching relation:

$$\beta_{\rm laser} = \beta_{\rm spp} + \frac{2\pi}{\Lambda_C} \tag{2}$$

[see scheme in Fig. 1(a)]. As an example, for a wavelength $\lambda = 7.5$ μm we obtain $\Lambda_C = 3.49$ μm [Fig. 1(c)]. Identical devices with and without grating couplers have been fabricated. For technological reasons we have implemented values of Λ_C of the order of 3Λ.

Figure 2(a) shows the measured laser output collected from one of the two cleaved facets of a typical device as a function of the injection current at room temperature (RT, 300 K). Lasing is obtained at a threshold current density of 5.5 kA/cm^2. The emission spectrum [Fig. 2(a), inset] exhibits a single mode emission at $\nu \approx 1320$ cm^{-1}, and therefore its normalized emission frequency is $\Lambda/\lambda = 0.158$. This allows us to identify the lasing mode as the one at the higher energy of the photonic band edge [see Fig. 1(b), inset]. The maximum of the electric field is
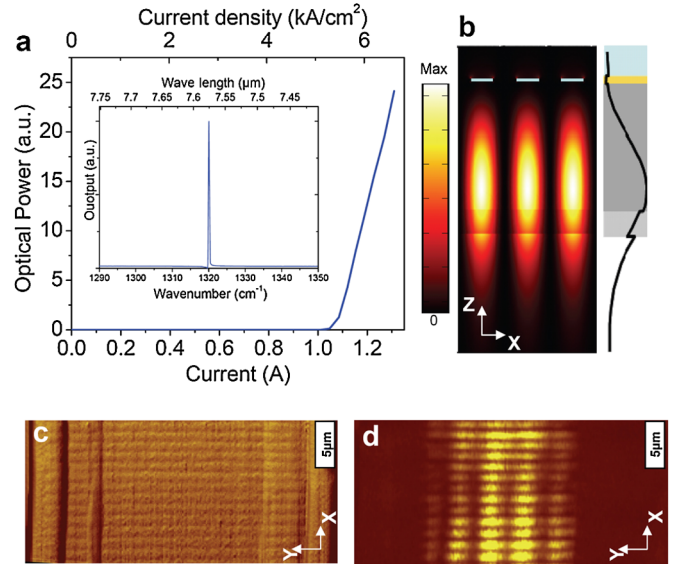
FIG. 2 (color online). (a) Light-current characteristics of a typical device, at RT (300 K). Inset: Typical emission spectrum at RT, at an injection current 50% higher than $I_{\rm th}$. The measurements have been performed in pulsed mode (50 ns pulses, 84 kHz), using a Fourier transform spectrometer with a LN$_2$-cooled HgCdTe detector. (b) Calculated field plot of the active laser mode in the device. The square modulus of E_z (arb. unit) is shown in a 2D color plot (left side). A 1D cross section is also provided (right side). The maximum of the electric field is localized in the active region, below the metallic fingers of the DFB grating. An evanescent electric field is present on top of the metallic fingers, indicating the presence of a hybrid SPP mode. (c) AFM topography of the 1st order DFB region. (d) a-NSOM image recorded simultaneously with the AFM image of panel (c). An evanescent electric field is clearly present on top of the metallic fingers which constitute the DFB grating.

localized under the fingers of the DFB grating, with a small portion leaking out above, as shown in Fig. 2(b) [7].

We have characterized the EM near-field distribution on various regions of the nanostructured metal top surface of the device. All the near-field maps are obtained using a home-built midinfrared a-NSOM [15] similarly to previous studies of QCLs [16]. The images are obtained by demodulating the optical signal at the second harmonic of the atomic force microscope (AFM) tip oscillation frequency Ω (details in supplemental material [12]).

Figures 2(c) and 2(d) show the AFM topography [panel (c)] and the corresponding near-field signal [panel (d)] acquired simultaneously in correspondence of the DFB grating regions, while the device was operated above threshold. A comprehensive experimental and theoretical study of the EM field distribution in QC lasers with metallic DFB gratings has been presented in Ref. [10]. The presence of an (evanescent) electric field detected on top of the metallic fingers confirms that lasing is achieved on a hybrid SPP mode: on the semiconductor side it profits from the active-region optical gain, while it leaks through the grating on top of the device surface.

Figure 3 reports the core result of the Letter. Two devices, one without (reference device, left panels), and with (SPP device, right panels) grating couplers, are studied. Panels (a) and (b) show their schematic cross sections. Panels (c) and (d) show AFM images of their top surfaces. The AFM images cover the passive sections—the 60-μm-long metallic strip—and also portions of the gratings, which are clearly visible at the left and right edges of the scans. The a-NSOM signal—i.e., the EM near field—is acquired simultaneously with the AFM

images with the devices in operation. The results [panels (e) and (f)] show that—while an a-NSOM signal is present on the grating surfaces in both cases—only the SPP devices present interference fringes which can be clearly distinguished on the metallic strip. The fringes stem from counterpropagating SPP excitations which travel on the surface of the metallic strip, with opposite wave vectors $+\beta_{\mathrm{spp}}$ and $-\beta_{\mathrm{spp}}$. Their presence proves that SPPs are generated and launched into the metallic waveguide. Furthermore, their absence in the reference device without couplers confirms that no light tunneling is possible through the top metallization.

Additional important information is the wavelength λ_{spp} of the plasmonic wave propagating on the passive metallic strip. Its value is experimentally measured by taking a 1D section of the a-NSOM and AFM signals in the center of the device. Figure 4(a) reports such a section, in correspondence of the white dashed line in Fig. 3(f). The topographic signal (green dotted curve) permits us to cor-
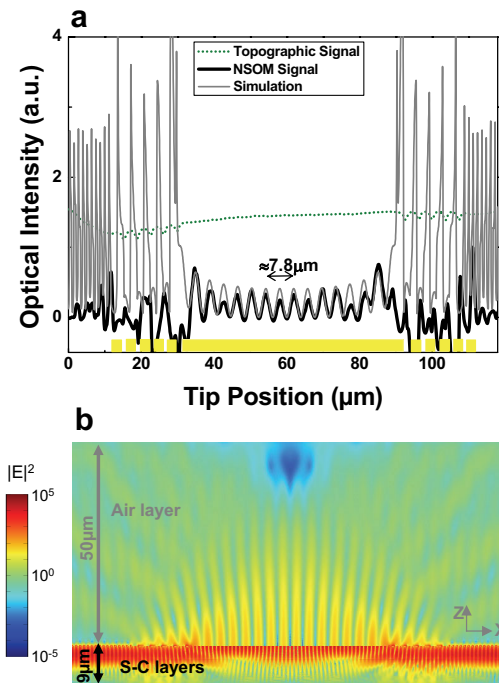
FIG. 4 (color online). (a) Intensity of the EM near field (a-NSOM signal) at the device top surface. The measured data (black curve) correspond to a 1D cross-section taken in correspondence of the dashed white line in Fig. 3(f). The numerical simulation (dark gray curve) is a 1D cross-section of Fig. 4(b) taken 100 nm above the metallic top-surface. The topographic signal (dotted green curve) allows one to correlate the EM near field with the top metallization. The standing wave on top of the passive metallic strip exhibits a clearly different periodicity with respect to the other portions of the device. In particular, the measurement yields $\lambda_{\mathrm{spp}} \approx 7.8 \ \mu$m, in excellent agreement with both the measured emission wavelength of the DFB laser portions and with the simulations. (b) 2D numerical simulation performed within a finite-element approach (details in supplemental material [12]). The color plot shows the electric field squared modulus $|\mathbf{E}|^2$ (arbitrary units) in logarithmic scale.

FIG. 3 (color online). Comparison between a device without coupler (left column), and with coupler (right column). (a), (b) Schematic structure of the devices. Without the grating coupler [panel (a)] the wave vector mismatch prevents efficient injection of SPPs into the passive central strip. The grating coupler [panel (b)] adapts the wave vectors, and it allows for efficient SPP launching. (c),(d) AFM images of the center of the devices. (e),(f) a-NSOM images. When the coupler is present, interference fringes are clearly present onto the passive region (the metallic strip) in the EM near field. When the coupler is missing, SPPs are clearly not injected into the passive section.

relate the a-NSOM one (black curve) with the surface metallization. The experimental data are in very good agreement with the simulations obtained within a finite-element approach (dark gray curve), which confirm that the couplers are crucial in order to inject the SPP wave into the passive waveguide. A sinusoidal fit of the near field onto the metallic strip yields a period of 3.89 μm, which corresponds to $\lambda_{spp} \approx 7.78$ μm. (Note: the a-NSOM signal in this region is proportional to the intensity, $|E_{near-field}|^2$.) This value is in good agreement with the wavelength measured in the far field [Fig. 2(a), inset]. This result further confirms the passive character of the metallic strip. If the detected evanescent field originated from light tunneling through the metal, its periodicity would reflect the light wavelength *inside* the laser and would yield $\lambda/(2n_{eff})$. This value is instead correctly measured in correspondence of the DFB regions, and it yields an estimate of $n_{eff} = 3.15$, in good agreement with the calculated effective index of the laser waveguide mode.

Note that the near-field signal is perturbed in correspondence of the couplers. This subtle effect—thoroughly discussed in supplemental material [12]—originates from coherent interference between the field radiated by the tip and the background field, which reaches the detector even in the absence of the tip. The measurements indicate therefore that a certain amount of background scattering is present at the junctions between the DFB grating and the passive sections.

Finally, two aspects deserve to be mentioned, although they are beyond the scope of this article: the coupling efficiency and the role of quasicylindrical waves (quasi-CW) [17]. The former aspect—the ratio between the power flux in the near field and the one impinging onto the coupler—becomes important when studying, for instance, a plasmonic circuit comprising an integrated source. This is part of the perspectives of this work, and will be tackled by optimizing the grating couplers. Initial theoretical results indicate that optimization of the coupler's parameters can lead to coupling efficiencies of a few percents. The role of cylindrical waves is a more complex issue. It has been shown that surface waves scattered by 2D slits in metallic surfaces include a contribution from SPP waves, but also from quasi-CW waves [8]. These are rapidly decaying waves with a free-space propagation constant, but bound to the metallic surface. In particular, SPPs and quasi-CWs tend to blend at long wavelengths, given the spatially extended character of SPPs. However, this has not prevented the use of "plasmonic" effects for the implementation of advanced device functionalities such as plasmonic collimators [18] and plasmonic polarizers [19]. The complex nature of the waves generated by our device can be seen in Fig. 4(b), which shows a 2D numerical simulation of a longitudinal cross section of the device. Note, in particular, the large spatial extension—as expected—of the surface waves above the central metallic strip. Our system can in fact be particularly valuable to elucidate the electromagnetic properties of metallic surfaces at long wavelengths, where the excitation of surface waves by optical means is highly inefficient [17].

*adel.bousseksou@u-psud.fr
†raffaele.colombelli@u-psud.fr

[1] T. W. Ebbesen, C. Genet, and S. I. Bozhevolnyi, Phys. Today **61**, No. 5, 44 (2008).
[2] S. Lal, S. Link, and N. J. Halas, Nat. Photon. **1**, 641 (2007).
[3] M. I. Stockman, Phys. Rev. Lett. **93**, 137404 (2004).
[4] E. Ozbay, Science **311**, 189 (2006).
[5] S. A. Maier, *Plasmonics: Fundamentals and Applications* (Springer, New York, 2007).
[6] J. Renger, R. Quidant, N. van Hulst, S. Palomba, and L. Novotny, Phys. Rev. Lett. **103**, 266802 (2009).
[7] A. Bousseksou, R. Colombelli, A. Babuty, Y. De Wilde, Y. Chassagneux, C. Sirtori, G. Patriarche, G. Beaudoin, and I. Sagnes, Opt. Express **17**, 9391 (2009).
[8] L. Aigouy, P. Lalanne, J. Hugonin, G. Julié, V. Mathet, and M. Mortier, Phys. Rev. Lett. **98**, 153902 (2007).
[9] S. Ravets, J. Rodier, B. Kim, J. Hugonin, L. Jacubowiez, and P. Lalanne, J. Opt. Soc. Am. B **26**, B28 (2009).
[10] A. Bousseksou, V. Moreau, R. Colombelli, C. Sirtori, G. Patriarche, O. Mauguin, L. Largeau, G. Beaudoin, and I. Sagnes, Electron. Lett. **44**, 807 (2008).
[11] M. Bahriz, V. Moreau, J. Palomo, R. Colombelli, D. Austin, J. Cockburn, L. Wilson, A. Krysa, and J. Roberts, Appl. Phys. Lett. **88**, 181103 (2006).
[12] See supplementary material at http://link.aps.org/supplemental/10.1103/PhysRevLett.104.226806 for design, fabrication, and a-NSOM details.
[13] M. Ordal, L. Long, R. Bell, S. E. Bell, R. R. Bell, R. Alexander, and C. A. Ward, Appl. Opt. **22**, 1099 (1983).
[14] D. M. Koller, A. Hohenau, H. Ditlbacher, N. Galler, F. Reil, F. R. Aussenegg, A. Leitner, E. J. W. List, and J. R. Krenn, Nat. Photon. **2**, 684 (2008).
[15] Y. De Wilde, F. Formanek, R. Carminati, B. Gralak, P. A. Lemoine, K. Joulain, J. P. Mulet, Y. Chen, and J. J. Greffet, Nature (London) **444**, 740 (2006).
[16] V. Moreau, M. Bahriz, R. Colombelli, P. A. Lemoine, Y. De Wilde, L. R. Wilson, and A. B. Krysa, Appl. Phys. Lett. **90**, 201114 (2007).
[17] P. Lalanne, J. Hugonin, H. Liu, and B. Wang, Surf. Sci. Rep. **64**, 453 (2009).
[18] N. Yu, J. Fan, Q. Wang, C. Pflugl, L. Diehl, T. Edamura, M. Yamanishi, H. Kan, and F. Capasso, Nat. Photon. **2**, 564 (2008).
[19] N. Yu, Q. Wang, C. Pflügl, L. Diehl, F. Capasso, T. Edamura, S. Furuta, M. Yamanishi, and H. Kan, Appl. Phys. Lett. **94**, 151101 (2009).
[20] See www.esf.org/euryi.